Experimental study of surface roughness effects on hydrodynamic characteristics of a submerged floating tunnel

Zou, P. X.; Ruiter, N.; Uijttewaal, W. S.J.; Chen, X. X.; Peters, D. J.; Bricker, J. D.

DOI
10.1016/j.apor.2023.103557

Publication date
2023

Document Version
Final published version

Published in
Applied Ocean Research

Citation (APA)
Zou, P. X., Ruiter, N., Uijttewaal, W. S. J., Chen, X. X., Peters, D. J., & Bricker, J. D. (2023). Experimental study of surface roughness effects on hydrodynamic characteristics of a submerged floating tunnel. *Applied Ocean Research*, *135*, Article 103557. https://doi.org/10.1016/j.apor.2023.103557

Important note
To cite this publication, please use the final published version (if applicable).
Please check the document version above.

Applied Ocean Research 135 (2023) 103557

Contents lists available at ScienceDirect

Applied Ocean Research

journal homepage: www.elsevier.com/locate/apor

Experimental study of surface roughness effects on hydrodynamic characteristics of a submerged floating tunnel

P.X. Zou [a,b,c], N. Ruiter [a], W.S.J. Uijttewaal [a], X.X. Chen [a], D.J. Peters [a], J.D. Bricker [a,c,*]

[a] Dept. of Hydraulic Engineering, Faculty of Civil Engineering & Geosciences, Delft University of Technology, Delft 2600GA, The Netherlands
[b] CCCC SFT Technical Joint Research Team, Zhuhai, Guangdong 519080, China
[c] Dept. of Civil and Environmental Engineering, University of Michigan, Ann Arbor, MI 48109, USA

ARTICLE INFO

Keywords:
Marine fouling
Hydrodynamic forces
Parametric shape
Roughness parameters
Submerged floating tunnel

ABSTRACT

Marine biofouling is a major concern in the operational performance of submerged floating tunnels (SFTs). The objective of this research is to investigate the effects of marine fouling (represented by surface roughness) on the hydrodynamic behavior of SFTs, including the hydrodynamic forces on the SFT subject to current-only, wave-only, and combined current-wave flow conditions. The effects of increased surface roughness induced by marine fouling on the dynamic response of an SFT are characterized by hydrodynamic force coefficients, including drag and inertia coefficients. At the Water Lab of Delft University of Technology (TU Delft), experiments have been performed in a wave-current flume to compare the SFTs' behaviors as affected by different roughness characteristics. In addition, a parametric cross-section for an SFT is presented, and the hydrodynamic performance associated with surface roughness effects on the parametric shape and circular SFT cross-section shape are compared. The results show that the parametric shape can effectively reduce the drag coefficient (C_d) under current-only conditions and lower the inertia coefficient (C_m) when waves are present. As roughness height and coverage ratio increase, C_d generally increases while C_m decreases. However, small differences in C_d and C_m can be observed with regard to roughness parameters for wave-only conditions. The Morison coefficients adapted for a marine-fouled SFT measured in the experiments are compared to predictions from engineering standards and are recommended for engineering practice.

1. Introduction

The submerged floating tunnel (SFT) is a new type of sea-crossing infrastructure holding promise to facilitate efficient and capable deep-sea transportation (Zou and Chen, 2021; Zou et al., 2020c, 2022). It is regarded as one of the alternatives to underwater tunnels and sea bridges for wide and deep sea-crossings. Due to its submergence depth (generally 20∼50 m Wikipedia 2023), the SFT has numerous advantages over traditional sea crossings, including its ability to avoid harsh wave and wind conditions or dense ship traffic. However, weeks to years following installation, an SFT is going to be colonized by marine species; this will be one of the key challenges for the SFT's operational effectiveness. Marine growth alters the hydrodynamic characteristics of an SFT by increasing its projected area, mass, and surface roughness. Further, it modifies the structure's properties, such as buoyancy weight ratio, which affects the mooring tension and natural frequency of the SFT and has a substantial impact on the reliability of the SFT. Moreover, the increased surface roughness can exacerbate flow instabilities, which significantly affect the hydrodynamic forces on the SFT and can reduce the service lifetime of the structure. In addition, concealment of the mooring lines and SFT exterior surfaces by marine fouling brings exceeding difficulty for structural inspection and maintenance.

Marine fouling is typically represented by surface roughness in the research, and the surface roughness effects on marine structures have been studied by a significant body of experimental research. Schoefs et al. (2022) presented an overview of research that examined biofouling of offshore structures. Marty et al. (2021b, 2021a) investigated the hydrodynamic behavior of a submarine cable, and used realistic mussel roughness models with different patterns and shapes applied to horizontal cylinders and exposed to currents, oscillating motions, and a combination of currents and oscillating motions. Furthermore, two types of hard roughness including mussels and corals were

---

* Corresponding author at: Dept. of Hydraulic Engineering, Faculty of Civil Engineering & Geosciences, Delft University of Technology, Delft 2600GA, The Netherlands.
E-mail address: jeremydb@umich.edu (J.D. Bricker).

https://doi.org/10.1016/j.apor.2023.103557
Received 29 December 2022; Received in revised form 28 March 2023; Accepted 29 March 2023
Available online 4 April 2023

experimentally studied and compared (Marty et al., 2022). Zeinoddini et al. (2016) examined the effects of surface roughness on the Vortex-Induced Vibration (VIV) of a circular cylinder for mechanical power harvesting using a towing tank tested on elastically mounted rigid cylinders. Sun et al. (2020) investigated the wake characteristics of cylinders with hemispherical surface roughness using Particle Image Velocimetry (PIV) measurement. Theophanatos and Wolfram (1989) conducted a set of experiments in a deep tank to investigate the effects of roughness height, roughness coverage percentages, and roughness type (Gravel, mussels, kelp) on the fluid loading of offshore structures. Henry et al. (2016) visualized wake structures of sand-roughened vertical cylinders in low Reynolds number flows.

Despite the extensive experimental research on hydrodynamic forces, flow instabilities, and dynamic response with respect to surface roughness, there are still many unanswered questions. Firstly, the prior research generally emphasized cross-sections with simpler shapes (e.g., circle and rectangle), and the shape comparison and optimization with respect to surface roughness has not yet been conducted. Zou et al. (2021a, 2020a, 2020b) proposed a parametric shape for an SFT to improve its hydrodynamic performance. Therefore, in this study, the influence of surface roughness on an SFT cross-section with the parametric shape is firstly experimentally investigated, and the hydrodynamic forces on SFTs with different cross-sections – namely, circular and the parametric shapes – under various hydrodynamic conditions are compared and evaluated.

Secondly, prior studies demonstrated that there is no universal agreement regarding the relationship between roughness parameters and hydrodynamic forces on a cylinder. According to Zhou et al. (2015) and Achenbach and Heinecke (1981), the presence of roughness promotes boundary layer transition, lowers the critical Re at which the drag crisis occurs, and can effectively reduce the mean drag and root mean square (RMS) lift coefficients. The surface roughness, on the other hand, has been shown to dramatically increase mean and fluctuating force coefficients, as noted by Henry et al. (2016), Marty et al. (2021b), and Walker et al. (2020). In addition, Theophanatos and Wolfram (1989) revealed that within a given range of relative roughness values, roughness height has a negligible effect on drag. The stark disparity can be attributed to the difference between the applied roughness scales and the experimental flow conditions. In addition, the contradiction of the results compared to existing studies can also be due to differences in the factors such as experimental set-ups (Zeinoddini et al., 2016), flow properties (Ribeiro, 1991), blockage ratio (Blackburn and Melbourne, 1996; Richter and Naudascher, 1976), aspect ratio (Theophanatos and Wolfram, 1989; West and Apelt, 1982), and Reynolds number ranges (Henry et al., 2016). Moreover, the definitions of equivalent diameter and relative roughness also play a significant role in the relationship between roughness parameters and hydrodynamic forces. Prior research characterized the roughness parameter by the roughness height k and a bulk cylinder diameter D (Henry et al., 2016; Jusoh and Wolfram, 1996; Marty et al., 2021b; Theophanatos and Wolfram, 1989; Zhou et al., 2015). Large-scale roughness, however, can effectively increase the flow blockage (i.e., equivalent diameter), the wake region in the vicinity of the cylinder, and consequently the drag coefficient. Furthermore, the definition of equivalent diameter is directly linked to key parameters such as force coefficients, Reynolds number (Re) and Keulegan–Carpenter number (KC). Therefore, the cylinder bulk diameter D may not be appropriate for a surface roughened cylinder, and an appropriate definition for an equivalent diameter has not yet been determined.

Thirdly, there are no specific research or engineering guidelines for hydrodynamic force coefficients that SFT research can refer to with consideration of marine fouling effects. Previous research about SFT hydrodynamic force prediction is mainly based on the Morison equation (Morison et al., 1950), where the drag and inertia coefficients were applied from other marine structures such as risers and pipelines. However, we should not simply apply the recommended values of force coefficients to the SFT from other marine structures due to the SFT's unique structural characteristics. On the one hand, the cross-section dimensions of the SFT are substantially larger than those of other marine structures, which results in a higher Re and lower KC number. Even in the case of extreme hydraulic events, the maximum KC number of an SFT can be lower than 0.23 (Yang et al., 2023), meaning there are limited references from which to find hydrodynamic force coefficients. Additionally, for a potential SFT application site such as the Qiongzhou Strait, the average water depth can be around 100 m, and the dimension of the SFT cross-section can be 20 m (depending on the number of tubes and traffic lanes). As a result, the blockage of a prototype SFT can reach 20% in situations where the blockage effect cannot be neglected. However, the effects of blockage on the hydrodynamic forces are not taken into account by existing standards. The applicability of hydrodynamic force coefficients in existing engineering standards should be carefully evaluated for SFTs.

Therefore, in order to address the aforementioned questions and fill in these knowledge gaps, the effects of surface roughness on the hydrodynamic forces on SFTs are experimentally investigated in this study. The hydrodynamic forces on SFT models with varying roughness height and coverage ratio are measured under uniform currents, regular waves, and combined current-wave flow conditions in the water lab of Delft University of Technology (TU Delft). Furthermore, two types of SFT cross-sectional shape (i.e., a parametric shape and a circular shape) have been tested to investigate the surface roughness effects for each cross-section shape. The paper is structured as follows. The experimental method, arrangement, and set-up of the SFTs are first described in Section 2. The result validation is then discussed in Section 3. Section 4 presents the test results for the influence of cross-section shape, roughness height, and roughness coverage ratio on the hydrodynamic forces on the SFT under current-only, wave-only and combined current-wave conditions. The comparison of the hydrodynamic force coefficients in this study with to those from existing standards is discussed in Section 5. A discussion of blockage effects is also presented.

2. Experimental work

2.1. Experimental set-up

The physical model tests are conducted in a wave-current flume at the Water Lab of Delft University of Technology with a length of 39 m, a width of 0.795 m and a height of 1 m. During the tests, a constant water level of 0.70 m is set to avoid spillage. Froude similitude with a scale of 1:50 is applied. For the wave conditions, a piston-type 2nd order wave generator with a maximum stroke length of 2 m is applied to generate the desired incident waves, equipped with an Automatic Reflection Compensation (ARC) system. At the flume end, a passive wave absorber is placed inside the flume to prevent wave reflection. A sharp-crested weir is placed at the end of the flume to control the water level.

Water surface elevation is measured by two arrays of wave gauges. In order to separate the incident and reflected waves, the least squares method proposed by Mansard and Funke (1980) is employed, and three wave gauges are placed to the front and back of the model to separate the reflected and incident waves. For flow velocity measurement, two electromagnetic velocity meters (Deltares type E30 EMS probe) are placed at the equal submergence depth as the SFT (0.35 m from the free surface), with longitudinal positions close to the SFT (assuming no flow disturbance due to the model) and far upstream, respectively. A third EMS is placed below the free surface at a depth of 0.2 m to measure the free stream velocity and check the uniformity of the current over the water depth. To measure the hydrodynamic force on the SFT, a 3-axis load cell from ME (K3D60a) is adopted with a maximal load range of ±100 N and an accuracy of 0.5% of full scale range. The load cell can measure the total horizontal and vertical forces on the SFT simultaneously. The data sampling frequency is 200 Hz with a block size of 2 data points. The load cell is mounted on a strip with one end connected to the mid-span of the SFT and the other end is clamped to the flume. Flow visualization is realized by injecting fluorescent dye upstream of the SFT. The injection location is at the mid-length of the SFT to reduce boundary effects from the side walls. Video records are taken with a Canon EOS 550D to capture the wake structures and flow separations. Before the tests, the load cell is calibrated by pulley tests, and numerous qualitative calibrations for the instruments are performed. The experimental set-ups are shown in Fig. 1.

2.2. Model fabrication

Prior experiments on an SFT with a rectangular cross-section subject to a current, regular waves and combined waves/currents have been performed at TU Delft (Drost, 2019). In order to further investigate the SFT cross-sectional shape effects on the hydrodynamic forces on the SFT, a circular shape and a parametric shape proposed by Zou et al. (2020a, 2021b) are selected for comparison. The heights of smooth SFTs (without roughness elements) with parametric and circular shapes are kept equal (0.16 m). In order to measure the force on the SFT and reduce wall effects, a clearance of around 2 cm between each end of the SFT and the flume wall is implemented (il Seo et al., 2015; Wu et al., 2021). 3D printing and a silicon mold are applied to create slices of each SFT with specific roughness elements. The mold is filled with epoxy, and after the solidification of each slice, the slices are assembled into a complete SFT model. Silicon sealant is used to combine the slices, and the two halves of the SFT are then filled with polyurethane foam for waterproofing. In order to fix the position of the extra weight added, the SFT model is filled with lightweight foam. The model mid-span is stiffly attached to a stainless-steel frame with a strip connected to the flume top rails. The SFT model is placed horizontally in the flume, with an additional weight tied on the strip to balance the buoyancy.

Modeling of marine fouling on an SFT is rather difficult, due to its dependence on time, space, and material, and uncertainties in the biological processes. A few attempts are conducted for modeling accuracy. For instance, Ameryoun et al. (2019) and Schoefs and Ameryoun (2013) used a probabilistic model; Marty et al. 2021b) reproduced a highly realistic representation of mussel colonization using 3D printing. Theophanatos and Wolfram (1989) embedded long kelp plants in the cylinders. However, in order to provide a basic and generalized understanding of surface roughness effects on hydrodynamic forces and flow characteristics of an SFT and to reveal the fundamental flow phenomena, in our study, the artificial marine fouling is modelled as uniform pyramid-shaped roughness, due to its simplicity and repeatability (Zeinoddini et al., 2016). The roughness elements are placed in a staggered arrangement, where the sheltering effect can be avoided. With the use of 3D printing technology, different shells are created to represent different roughness cases. The roughness elements are applied to the entire surface of the SFT. The pyramids are designed with a base to height ratio of 2:1. Two roughness heights are chosen (i.e., 15 mm and 5 mm), and two roughness coverage ratios including 100% and 50% are included to investigate the three-dimensional impacts of surface roughness. Therefore, six SFT models are fabricated, shown in Fig. 2. The main characteristics of the models are shown in Table 1. The definitions of k_s, D_{ex} and D_{ez} can be found in Eqs. ((2)~(5).

2.3. Test cases

A series of tests are conducted with different current and wave characteristics. The SFT models are subjected to a current-only, a wave-only, and a combined current-wave condition. These different environments consist of various current velocities, wave heights, and wave periods, and the combination of these parameters is tested on each model. The generated waves had heights of up to 0.16 m and wave periods of up to 1.84 s. Currents are generated with a maximum current speed of 0.3 m/s. The free-stream turbulence intensity is around 4% of the mean flow speed in the current-only cases (Zou et al., 2023). For the wave-current combined conditions, currents are generated first, and waves are then superimposed onto the current. The test conditions are listed in Table 2.

The quality of the generated currents and waves is listed in Table 3.

Based on Froude scaling in Eq. (1), the upper limit values of the environmental conditions at prototype scale are calculated in Table 4.

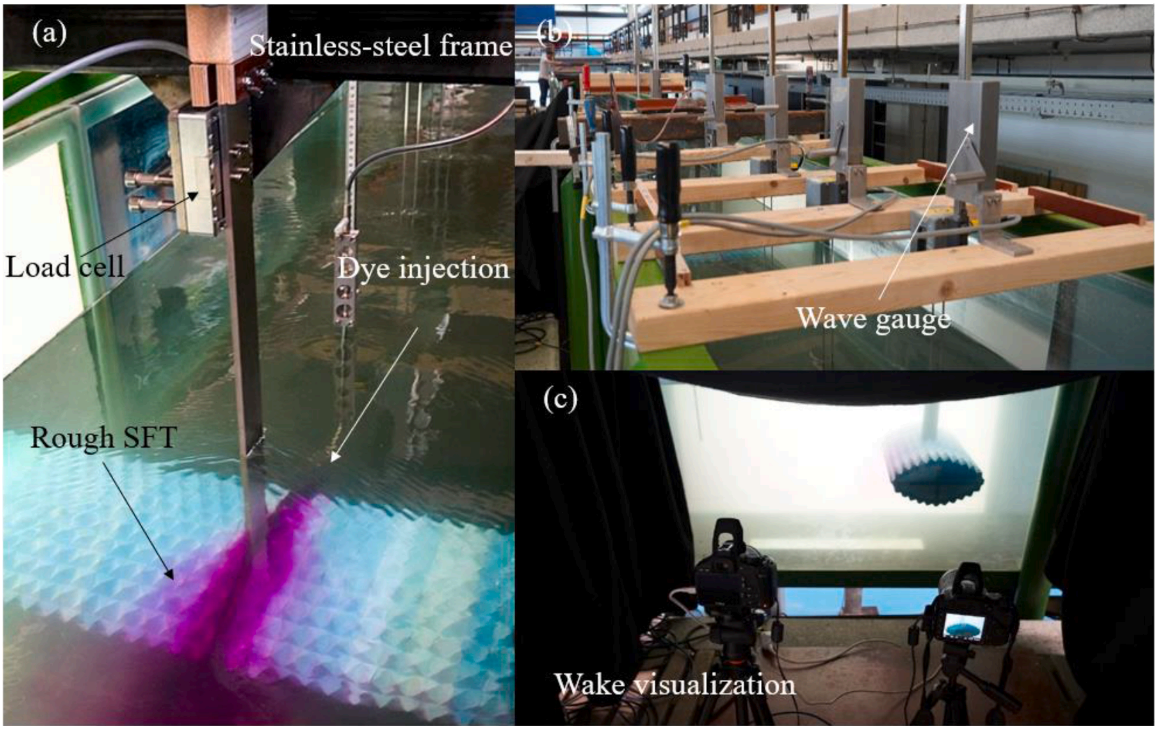

Fig. 1. Experimental apparatus. (a) Load cell attached to the SFT model, suspended from a stainless-steel frame, with upstream dye injection for wake visualization (purple area); (b) two arrays of wave gauges (six gauges) placed at each side of the model; (c) Two video records to capture the wake structures and flow separations.

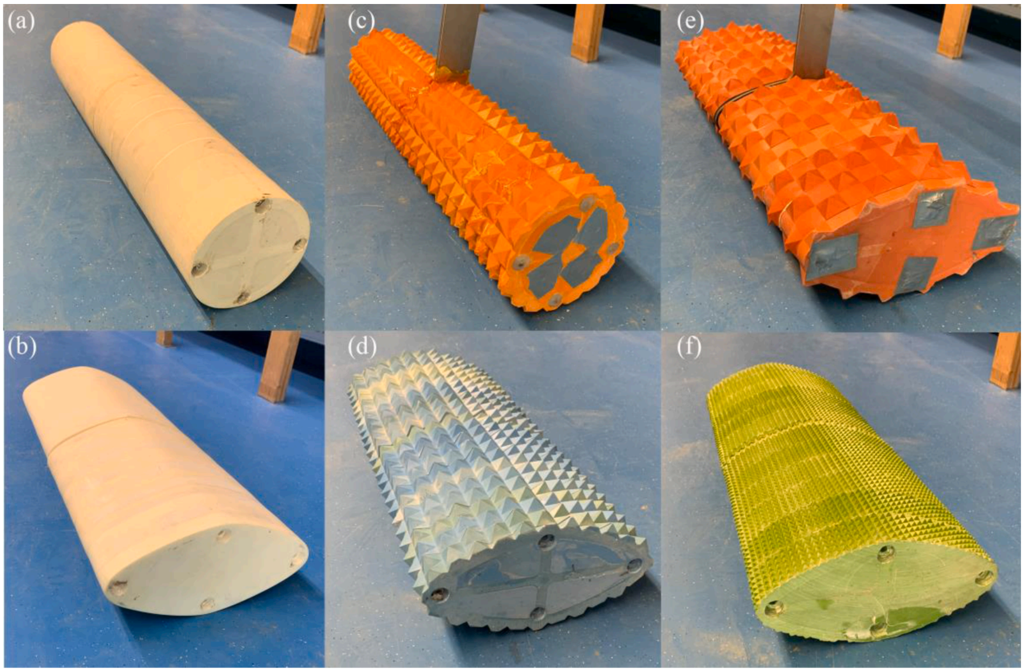

Fig. 2. Six SFT configurations. (a) CS; (b) PS; (c) CR; (d) PR; (e) PR50; (f) PRS.

Table 1
Main characteristics of the modelled SFT and artificial marine growth.

Model	Cross-section shape	Surface	Roughness height k (m)	Coverage ratio (%)	k_s (m)	D_{ex} (m)	D_{ez} (m)
CS	Circular	Smooth	0	0	0	0.16	0.16
CR	Circular	Rough	0.015	100	0.0075	0.175	0.175
PS	Optimized	Smooth	0	0	0	0.16	0.32
PR	Optimized	Rough	0.015	100	0.0075	0.175	0.335
PR50	Optimized	Rough	0.015	50	0.00375	0.1675	0.3275
PRS	Optimized	Rough	0.005	100	0.0025	0.165	0.325

Table 2
Environmental conditions used in the experiments.

Environment	Label	Current Velocity (m/s)	Wave Height (m)	Wave Period (s)
Current-only	C1	0.1	–	–
	C2	0.2	–	–
	C3	0.3	–	–
Wave-only	W1	–	0.08	0.92
	W2	–	0.08	1.12
	W3	–	0.08	1.41
	W4	–	0.08	1.84
	W5	–	0.12	1.84
	W6	–	0.16	1.84
Combined current-wave	CW1	0.2	0.08	0.92
	CW2	0.2	0.08	1.12
	CW3	0.2	0.08	1.41
	CW4	0.2	0.08	1.84
	CW5	0.2	0.12	1.84
	CW6	0.2	0.16	1.84
	CW7	0.3	0.16	1.84

$$\lambda L_m = L_p,\ \lambda H_m = H_p,\ \sqrt{\lambda}T_m = T_p,\ \sqrt{\lambda}U_m = U_p \tag{1}$$

where, λ is model scale (here $\lambda = 50$); The subscript m represents for model and p represents for prototype; L is length; H is wave height; T is wave period; U is freestream velocity and is calculated from the mean values of both EMS probes at the SFT depth.

Table 3
Generated current and wave characteristics.

	Average current velocity U (m/s)	Standard deviation of U (m/s)
C1	0.100	0.004
C2	0.200	0.008
C3	0.300	0.011

	Average wave period T (s)	Standard deviation of T (s)	Average wave height H (m)	Standard deviation of H (m)
W1	0.920	0.003	0.075	0.004
W2	1.121	0.002	0.079	0.013
W3	1.411	0.003	0.081	0.023
W4	1.841	0.003	7.994	0.006
W5	1.844	0.002	0.012	0.009
W6	1.844	0.002	0.016	0.041

Table 4
Environmental conditions at model and prototype scales.

	Model scale	Prototype scale
SFT height (m)	0.16	8.00
Submergence depth (m)	0.35	17.50
Wave height (m)	0.16	8.00
Wave period (s)	1.84	13.01
Current velocity (m/s)	0.30	2.12

2.4. Performance metrics

As aforementioned, various definitions of roughness can be found from the prior literature, and no definite consensus on the roughness parameter determination can be achieved. Further, marine fouling is highly reliant on time, space, organism types (e.g., hard fouling, soft fouling), geometry, and material properties, and different roughness parameters have varying effects on the hydrodynamic forces on the structures. According to Schultz (2007) and Demirel et al. (2017), the consequences of marine fouling differ depending on the roughness coverage ratio. The skewness and arrangement of the roughness elements can also have an impact on the force coefficients and critical Reynolds number, shown in Fuss (2011) and Zou et al. (2023). However, there is no universal roughness function that applies to all types of roughness, and the question of how to correlate the roughness functions of fouled surfaces with quantifiable metrics is a question far from being answered. Given that the effects of multiple roughness types are non-linear and strongly correlated with flow regimes and instabilities, it is challenging to correlate different types of fouling surface roughness with quantifiable metrics (Ribeiro, 1991). In this study, we propose the equivalent diameter, which is determined by an equivalent blockage area. For a three-dimensional object, this is a way to parameterize the actual blockage area. This method can take into account 3-dimensional roughness distributions with a wide range of roughness parameters such as roughness height, geometry, coverage ratio, skewness, kurtosis, and flatness. The equivalent diameter determined by an equivalent blockage area is given by

$$D_{ex,ez} = D_{x,z} + 2k_s \tag{2}$$

where, $D_{x,z}$ is the bare SFT dimension; Typically, the frontal area projected onto a plane normal to the direction of flow is used as the reference area for drag coefficient calculations. On the other hand, the planform area, which is visible from above in the direction normal to the bluff body, is used for lift coefficient calculations (Mansard and Funke, 1980); the SFT height D_x is used for the drag coefficient while the SFT chord length D_z is used for the lift coefficient; With the equivalent diameter, the objective is to find a quadrangle that has the same blockage cross-sectional area as the original repetitive roughness elements, shown in Fig. 3.

Thus, the reduced roughness height k_s can be calculated by:

$$k_s = \frac{\sum_i S_i}{l} \tag{3}$$

where, S_i is the aera of a single roughness element; i is the number of repetitive roughness elements.

The effects of surface roughness on the dynamic response of a submerged floating can be characterized by hydrodynamic forces and their dimensionless coefficients. For current-only conditions, the in-line drag force is given by

$$F_d = \frac{1}{2}\rho C_d U^2 D_{ex} \tag{4}$$

where, F_d is the time-averaged drag force per unit of length; C_d is the mean drag coefficient of the SFT; D_{ex} represents the equivalent diameter of the SFT for the drag; ρ is fluid density.

Similarly, the lift force of the SFT under current-only conditions is defined as

$$F_l = \frac{1}{2}\rho C_{l,rms} U^2 D_{ez} \tag{5}$$

where, F_l is the root mean square (RMS) fluctuating lift force per unit of length; $C_{l,rms}$ is the RMS fluctuating lift coefficient; D_{ez} represent equivalent diameter of the SFT for the lift.

According to the Morison equation, the hydrodynamic force acting on the SFT in the in-line direction is given by

$$\begin{aligned} F &= F_d + F_m + F_p = \frac{1}{2}\rho C_d D_e U|U| + \rho C_A A_e \dot{U} + \rho A_e \dot{U} \\ &= \frac{1}{2}\rho C_d D_e U|U| + \rho C_m A_e \dot{U} \end{aligned} \tag{6}$$

where, F_m and F_p represent the hydrodynamic-mass force and the Froude–Krylov force, respectively, which together are called the inertia force; A_e is equivalent cross-sectional area of the SFT (considering surface roughness); $\dot{U}$is fluid acceleration; C_A is hydrodynamic-mass coefficient; $C_m = C_A + 1$, which is the inertia coefficient.

The Morison equation is originally intended for vertical cylinders, and thus, needs to be modified for horizontal cylinders. The horizontal and vertical directions are assigned as two force coefficients for the horizontal cylinder in the modified Morison equation. The validity of the modified Morison equation was proved by Chaplin (1988), and it has been widely applied such as in Bai et al. (2017). Therefore, the modified Morison equation is used to describe the hydrodynamic forces acting on the SFT, given by

$$F_i = \frac{1}{2}\rho C_{di} D_{ei} U_i \sqrt{U_x^2 + U_z^2} + \rho C_{mi} A_e \dot{U}_i \tag{7}$$

where, F_i represents the hydrodynamic force on the SFT per unit length; $i, j = x, z$ represents the horizontal and vertical direction, respectively.

For wave-only and combined current-wave conditions, the drag and inertia coefficients were calculated by the least squares method, which solves the joint Eqs. (8)~(11), given by

$$f_{di} \sum \left[U_i^2 \left(U_x^2 + U_z^2\right)\right] + f_{Mi} \sum \left(U_i \sqrt{U_x^2 + U_z^2}\, \dot{U}_i\right) = F_{ti} \sum \left(U_i \sqrt{U_x^2 + U_z^2}\right) \tag{8}$$

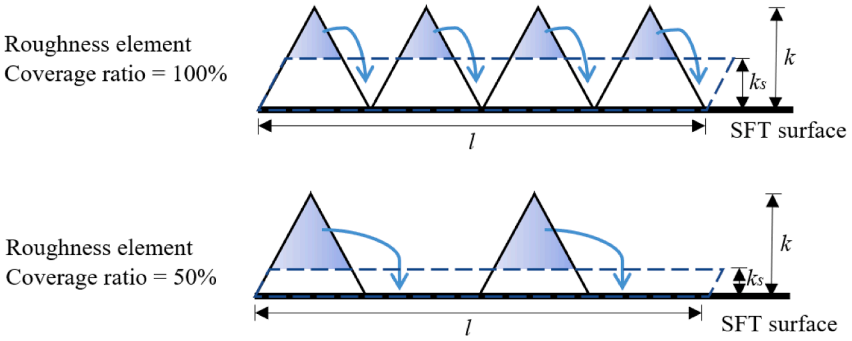

Fig. 3. Typical roughness patterns and reduced roughness height. k is the actual roughness height; k_s is the reduced roughness height with an equal blockage area; l is the length of the repetitive roughness patterns.

$$f_{di}\sum\left[U_i\sqrt{U_x^2+U_z^2}\,\dot{U}_i\right]+f_{Mi}\sum\left(\dot{U}_i^2\right)=F_{ti}\sum\dot{U}_i \tag{9}$$

$$f_{di}=\frac{1}{2}\rho C_{di}D_{ei} \tag{10}$$

$$f_{mi}=\rho C_{mi}A_e \tag{11}$$

where, F_t is the force per unit length on the SFT measured by the load cell.

Due to the low KC value under wave-only and combined current-wave conditions, the hydrodynamic force is highly inertia dominated, and hence, the lift force will be negligible. In terms of considering hydrodynamic characteristics and flow properties, several key parameters should be considered. For current-only cases, the Reynolds number (Re) is presented as a function of normalized coefficients, given by

$$\mathrm{Re}=\frac{\rho U D_{ex}}{\mu} \tag{12}$$

where, μ is fluid dynamic viscosity. The Strouhal number St is a dimensionless number describing oscillating flow mechanisms (e.g., vortex shedding). The definition of St in this study is given by

$$\mathrm{St}=\frac{fD_{ex}}{U} \tag{13}$$

where, f is the frequency of vortex shedding.

For the wave-only cases, Keulegan–Carpenter number (KC) is applied and defined as

$$\mathrm{KC}_i=\frac{U_{mi}T}{D_{ej}} \tag{14}$$

where U_m is the maximum orbital velocity of waves at the half water depth (same depth as the SFT) in both wave-only and wave-current flows; T is wave period; The equivalent diameter of the SFT under waves is defined as the blockage length projected in the direction of flow oscillation (Rusch et al., 2020); Therefore, De_z is used to calculate KC_x, and De_x is used to calculate KC_z.

For combined current-wave conditions, multiple key parameters were proposed for assessing the consistency of the data from the prior literature. The dimensionless parameter "current-wave velocity ratio" U/U_0 is an important criterion for determining the hydrodynamic force coefficients and was adopted as in Chandler and Hinwood (1982). In addition, although the KC number is questionable and ambiguous when currents are present, it is nonetheless commonly adopted as the main metric. For instance, Iwagaki and Asano (1985) compared two KC number definitions in the combined wave-current field and found that KC $=\pi UT/D$ ($U > U_m$) has a good agreement with the KC versus hydrodynamic force relations developed in wave-only circumstances. KC $= (U+U_m)T/D$ was employed in Sarpkaya and Isaacson (1981) which found that in this way, the regimes of vortex patterns can be described in an orderly manner (Zdravkovich, 1996). In addition, KC $= U_mT/D$ was applied in Fredsoe and Sumer (2006) for combined current-wave cases.

In this research, in order to show the variation of kinematics as currents superposed on waves, the vector sum of flow velocity is used for the definition of KC under combined current-wave conditions, given by

$$\mathrm{KC}_x=\frac{(U_{mx}+U)T}{D_{ez}} \tag{15}$$

$$\mathrm{KC}_z=\frac{U_{mz}T}{D_{ex}} \tag{16}$$

2.5. Comparison with previous experiments

The hydrodynamic forces on the SFT should be verified to confirm the accuracy of the experimental set-up and measurements. Therefore, in this section, the results from the smooth circular SFT (CS) are discussed and compared against experimental data from the literature.

Comparisons of C_d, $C_{l,rms}$, and St against the results from the literature (Schewe, 1983) are shown in Fig. 4. Error bars correspond to the standard deviations of the coefficients. It shows that the measured $C_{l,rms}$ matches well with prior experiments. However, in the selected range of Reynolds numbers, the measured C_d and St are much higher than in the literature. The discrepancy of C_d is up to 50% compared to the prior experiments. This discrepancy can be attributed to the large blockage ratio of the SFT applied in this study (the ratio of diameter over water depth is 23%). According to West and Apelt (1982), a blockage ratio higher than 6% leads to a distortion of the flow where the blockage effects can be significant. It is well known that the drag force coefficients (both mean and fluctuating) and Strouhal number increase with increasing blockage ratio in the subcritical regime (Blackburn and Melbourne, 1996; Richter and Naudascher, 1976). Therefore, a blockage ratio correction procedure is needed and the C_d is corrected by using Eq. (17), proposed by Allen and Vincenti (1944) .

$$\frac{C_d'}{C_d}=1-\frac{1}{2}C_d\left(\frac{D}{h}\right)-2.5\left(\frac{D}{h}\right)^2 \tag{17}$$

where, C_d' is the corrected value of the mean drag coefficient of the SFT; D is the SFT diameter; h is water depth.

Similarly, Roshko (1961) showed that the correction for Strouhal number (St) can follow the same way, given by

$$\frac{\mathrm{St}'}{\mathrm{St}}=1-\frac{1}{2}\mathrm{St}\left(\frac{D}{h}\right)-2.5\left(\frac{D}{h}\right)^2 \tag{18}$$

where, St' is the corrected value of the Strouhal number.

This method is reliable for flow regions where the drag coefficient is not highly Reynolds dependent, which is the case for the selected Re range in this study. Fig. 4 shows that the corrected C_d and St show good agreement with the literature, which concludes that the experimental set-up and measurements are providing accurate results.

However, a simple blockage ratio correction procedure can hardly be applied correctly in all flow regimes since the actual shape of the pressure distribution changes with blockage West and Apelt, 1982). In addition, the applicability of Eqs. (17) and ((18) to rough SFTs is doubtable since the pressure distribution on the SFT surface changes with surface roughness. Therefore, the uncorrected drag coefficients are used in the following section.

3. Surface roughness effect on SFT loads

In this section, the experimental results of the SFT with different configurations under the current-only, the wave-only, and the combined current-wave conditions are present. Influential factors including SFT cross-section shape, roughness height, and roughness coverage ratio are examined in detail. For the current-only conditions, the mean drag coefficient C_d, the RMS lift coefficient $C_{l,rms}$, and the Strouhal number St are analyzed. For the wave-only and the combined current-wave conditions, the drag and inertia coefficients are investigated and derived by the least squares method.

3.1. Current-only conditions

3.1.1. Effects of cross-section shape

The circular and parametric shapes for the C_d of the smooth and the rough SFT sets are shown in Fig. 5. The equivalent diameter of the circular and parametric shapes is equal in each set. Due to a more streamlined shape, the parametric shape SFTs of both sets have lower drag coefficients than their circular counterparts in the selected Re range. Compared with the circular cross-section, the parametric shape has around a 30% reduction of C_d for the smooth set, but the reduction

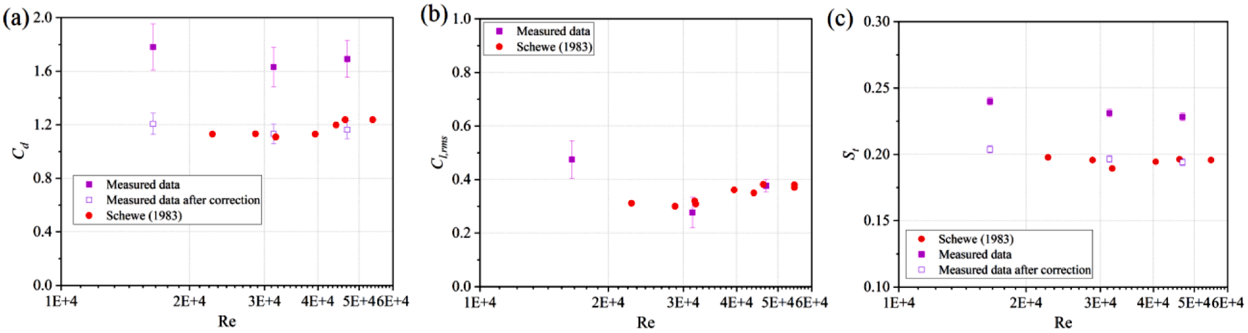

Fig. 4. Comparison between measured parameters in this study and the prior literature, as a function of Re. (a) Drag coefficient; (b) RMS lift coefficient; (c) Strouhal number.

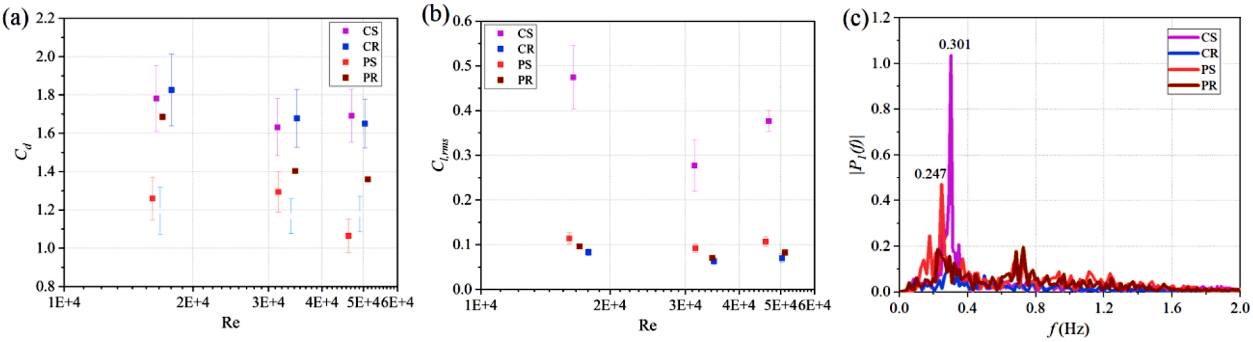

Fig. 5. Distribution of C_d, $C_{l,rms}$, and $|P_l(f)|$ from direct force measurements for the SFT configurations CS, CR, PS, and PR, under current-only conditions. (a) Drag coefficient; (b) RMS lift coefficient; (c) Lift force frequency spectrum.

turns out to be around 16% for the rough set (Fig. 5(a)). This indicates that, although the parametric shape still exhibits preferable hydrodynamic performance over the circular shape, the drag reduction caused by shape optimization is less influential in the presence of surface roughness.

Fig. 5(b) shows that the $C_{l,rms}$ of the CS is much larger than the other three configurations in the selected Re range. In addition to the smooth circular shape, the $C_{l,rms}$ of the PS and rough SFTs is rather low (around 0.1). The lift force is measured along the SFT span, and the vortex shedding in the turbulent wake regime occurs non-uniformly and incoherently in cells. Due to the effects of low spanwise correlation, the fluctuating lift is lower than expected.

Fourier transforms of the lift signals for each case with $U = 0.2$ m/s are shown in Fig. 5(c). A distinct peak frequency (f = 0.301 Hz) is present in the CS configuration, which represents the vortex shedding frequency. The lift spectrum of the CS has a much higher amplitude than the PS and the rough configurations. Multiple peaks can be observed in the PS configuration, and the peak frequency with the largest lift spectrum amplitude is 0.247 Hz. The lift spectrum amplitudes are significantly smaller for the rough configurations than for their smooth counterparts.

It is noteworthy that the peak frequency for the circular shape (f = 0.301 Hz) is higher than that of the parametric shape (f = 0.247 Hz). This may be attributed to the fact that with the large blockage and bottom wall interaction effects, the upstream flow acting on the SFT is asymmetric, causing the angle of attack to be non-zero, thereby generating a vertical component of flow behind the SFT. Therefore, the vortex shedding frequency is associated with the horizontal dimension of the SFT as well, and the parametric shape may generate longer vortices due to its larger horizontal dimension.

The morphology of the vortex street at $U = 0.2$ m/s (Re = 32,000) for the smooth circular and parametric shapes are compared in Fig. 6, to examine the vortex shedding characteristics of the two shapes and determine the mechanisms underlying the lift force spectrum. The sequence of movie frames generally covers one vortex-shedding period. The dye gets swept into vortices and forms coherent structures as they move downstream away from the SFT. The locations of concentrated vorticity are illustrated by the substantial coherent structures. At $T = 0$ s with the circular shape, the vortex is generated at the top surface of the SFT in the recirculation zone and moves from the upper to the lower side

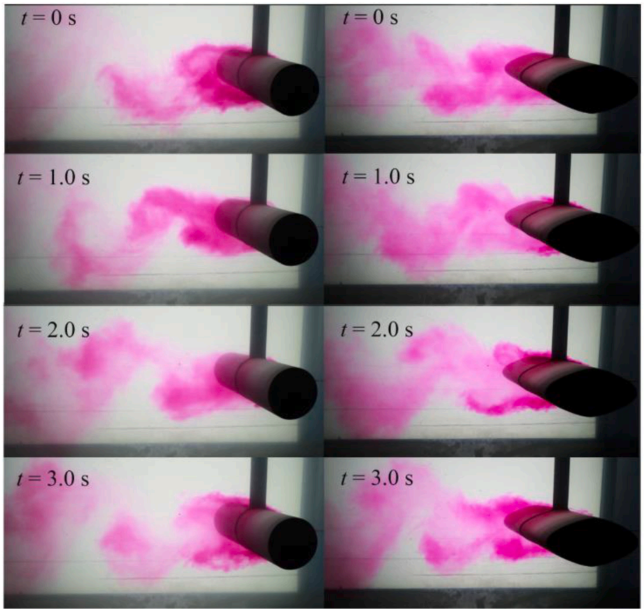

Fig. 6. Time series of flow visualization at Re = 32,000 for CS (left) and PS (right).

behind the SFT. At $T = 1$ s, the vortex begins to form at the lower side as the upper recirculation zone is pushed away from the SFT. As the vortex at the bottom side detaches from the SFT, the low-pressure vortex is pushed away and shed downstream at $T = 2$ s, and a new vortex emerges at the top surface of the SFT at $T = 3$ s. These vortices spread as the wake widens, and a periodic steady-state shedding of the vortices is found. Therefore, vortices detach periodically from either side of the body, forming a Kármán vortex street, leading to an oscillating force that acts on the SFT (i.e., fluctuating lift force), and a clear vortex shedding frequency peak can be seen in Fig. 5(c). However, the parametric shape experiences more vortex interference (T = 0 s and 1.0 s). The shear layers separate from the SFT, roll-up, and reattach to the leeward surface of the SFT (T = 2.0 s). Due to the less coherent vortex structures and turbulent behavior of the vortex formations, the lift spectrum amplitude is significantly reduced, as illustrated in Fig. 5(c).

3.1.2. *Effects of roughness height and coverage ratio*

To investigate the influence of roughness height and coverage ratio, the parametric shape with the PR (roughness heights of 15 mm, roughness coverage ratio of 100%), PRS (roughness heights of 5 mm, roughness coverage ratio of 100%) and PR50 (roughness heights of 15 mm, roughness coverage ratio of 50%) are compared. Fig. 7(a) demonstrates that the PR has the largest drag coefficient, while there is less of a clear distinction between the PRS and PR50. It can be concluded that C_d increases with increasing roughness height and coverage ratio. However, since the roughness substantially suppresses vortex shedding for the three configurations, no discernible difference can be seen for in $C_{l,rms}$ (Fig. 7(b)). Fig. 7(c) shows the lift force of the parametric rough configurations in the frequency domain. Multiple frequency peaks can be observed in all the rough configurations, which indicates that the surface roughness lessens the vortex shedding and homogenizes the turbulent flow. Comparing the PRS to the PR configuration, it is evident that the highest lift spectrum amplitude decreases with increased roughness height. Comparing the PR50 with the PR configuration, the effect of the roughness coverage ratio on the highest lift spectrum amplitude is not noticeable.

3.2. *Wave-only conditions*

3.2.1. *Effects of cross-section shape*

The drag and inertia coefficients of the circular and parametric shapes (with the smooth and the rough SFT sets) are displayed in Fig. 8. The hydrodynamic force coefficients in the horizontal and vertical directions are shown as a function of KC. This shows that for all the configurations, the horizontal drag coefficients increase exponentially as KC decreases. $C_{d,x}$ reaches 70 at KC = 0.14 for the parametric shape. Due to the small KC value in the test conditions, inertia dominates the total force compared to the drag, and a slight error in time shift of the signals can result in a dramatic change of C_d, which is corroborated by the range of the error bars. The C_d computation can be contaminated by phase shift errors.

Teng (1983) proposed an indicator RR (RR = 0.101KC for waves in deep water) to examine the reliability of the measured hydrodynamic force coefficients in wavy flow and concluded that only for RR >8 can the data be better conditioned to predict $C_{d,x}$. With decreasing KC, the error bar span can reach over 30% of the measured value at KC = 0.14 (W1 case, Table 2). The experimental data is therefore poorly conditioned for resolving drag coefficients.

In order to minimize the effects of error bars on the results, the $C_{d,x}$ of only cases W4∼W6 (Table 2) are presented in the subplot of Fig. 8(a). The $C_{d,x}$ of both rough configurations is larger than their smooth counterparts, and among the four SFT configurations, the PR has the largest $C_{d,x}$. This can be attributed to the parametric shape's longer perimeter and more surface roughness elements, which cause a larger frictional drag than the circular shape. It should be noted that the horizontal dimension of the parametric shape is larger than the circular shape, which results in a smaller KC_x value for the parametric shape under identical wave conditions. However, with an equal blockage height, KC_z is the same for the two cross-section shapes (Fig. 8(b)). It shows that the parametric shape (in both rough and smooth sets) has a larger $C_{d,z}$ than the circular shape because the longer horizontal dimension increases the vertical drag. Contrarily, the difference in $C_{d,z}$ is not obvious for the same cross-section shape. It appears that with increasing KC_z, the $C_{d,z}$ declines abruptly before remaining constant, leveling off at about $KC_z = 0.6$. Note that the $C_{d,z}$ of the circular SFTs can take negative values. This is likely because the vertical drag force component is rather small at the low KC values, the $C_{d,z}$ computation is therefore highly sensitive to the time shift of the measured force signals, and thus, generates a large error.

The circular and parametric shapes for the $C_{m,x}$ of the smooth and the rough SFT sets are shown in Fig. 8(c). It demonstrates that the parametric shape SFT has a significantly lower $C_{m,x}$ than the circular shape (around a 30% reduction). The circular shape exhibits a slight decrease in inertia coefficient with increasing KC, while the parametric shape has a moderate increase followed by a marked reduction with a maximum at about KC = 0.7. The PR has a lower $C_{m,x}$ compared to the PS, whereas the difference of $C_{m,x}$ between the CR and CS is less prominent. The presence of the exaggerated surface roughness decelerates the incoming flow, and hence, lowers the inertia force and coefficient. Prior literature has shown that the inertia can be reduced by surface roughness (Justesen, 1989). Due to the more streamlined geometry of the parametric shape and longer perimeter with more roughness elements, the attached flow on the SFT surface undergoes increased fluid-roughness interaction and momentum transformation. This inertia reduction effect is therefore more noticeable for the parametric shape.

On the contrary, due to a longer chord length, the SFT's horizontal cross-section area that is subject to waves grows. As a result, $C_{m,z}$ is larger for the parametric shape than the circular shape (Fig. 8(d)).

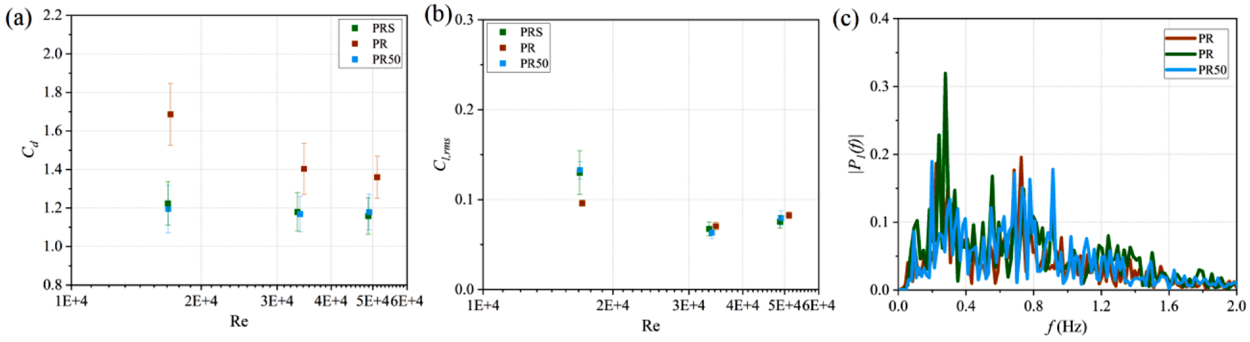

Fig. 7. Distribution of C_d, $C_{l,rms}$, and $|P_l(f)|$ from direct force measurements for SFT configurations PRS, PR, and PR50, under current-only conditions. (a) Drag coefficient; (b) RMS lift coefficient; (c) Lift force frequency spectrum.

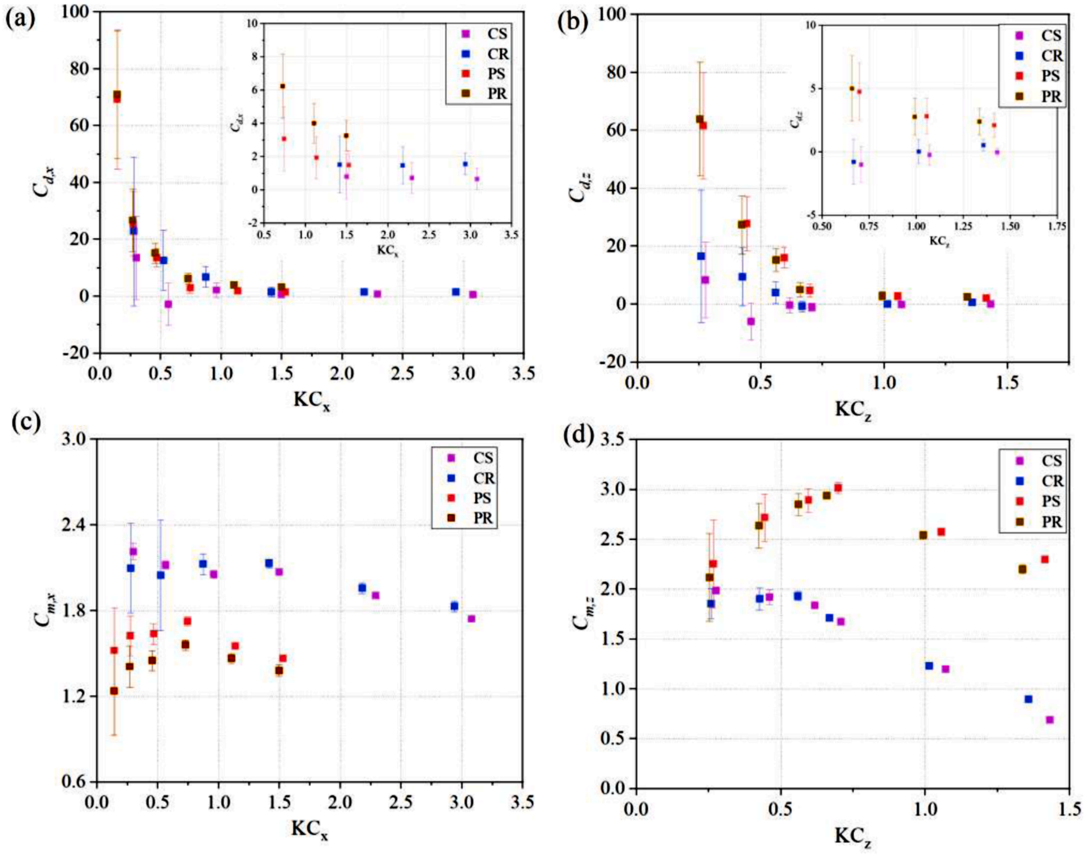

Fig. 8. Distribution of drag and inertia coefficients as a function of the Keulegan–Carpenter number KC (in the horizontal and vertical directions) for the SFT configuration CS, CR, PS, and PR, under wave-only conditions.

Additionally, in contrast to the horizontal inertia coefficients, the vertical inertia coefficients drop more rapidly with increasing KC. The maximum at $KC_z = 0.6$ in $C_{d,z}$ is illustrated in $C_{m,z}$, where a fairly constant value followed by a sharp decline is observed for the circular shape. However, for the parametric shape, the maximum $C_{m,z}$ moves to around $KC = 0.7$ with a gradual increase and a sharp decrease. These maxima stem from the change in wave height (see Table 2), indicating that the hydrodynamic force coefficients are more sensitive to wave height than the wave period. Contrary to $C_{m,x}$, $C_{m,z}$ does not clearly distinguish between the rough and smooth configurations for either shape. Intriguingly, the declining trend of the $C_{m,z}$ has a steeper slope (more sensitive) than the $C_{m,x}$ as a function of KC.

It should be noted that the smooth SFT has a larger $C_{m,x}$ than the rough case, but there is no distinct difference in $C_{m,z}$ between the smooth and rough cases. Contradictory results can be observed, as in Marty et al. (2021b), where the inertia coefficient of the smooth cylinder is lower than the rough case. This can be attributed to the fact that in Marty et al.'s (2021b) experiments, the oscillating and periodic motion of flow is created by towing a hexapod connecting the cylinder. Similarly, planar oscillatory flow, generated by a towing tank or a U-shape tube, is widely applied to investigate the hydrodynamic force coefficients under waves (Konstantinidis and Bouris, 2017; Pearcey et al., 2017; Skomedal et al., 1989). The oscillating planar flow can kinematically represent the horizontal component of the orbital velocity of waves, however, dynamically, there is a difference. The hydrodynamic mass force caused by the body-generated disturbance flow can be represented, but the Froude–Krylov force of the inertia associated with the absolute flow acceleration is not included. This leads to a difference in the boundary layer development and pressure gradient on the cylinder as compared to realistic waves. This difference presented in the flow around the cylinder affects the hydrodynamic forces (i.e., inertia) acting on the cylinder, and the Morison equation's weighting of the drag and inertia components is incorrect due to the difference in the forcing mechanism. For circumstances where inertia is dominant (small KC), as in this SFT study, this effect is more significant.

In addition, for vertical cylinders, the vertical force component parallel to the cylinder axis can be negligible. However, for horizontal cylinders, the vertical component due to the orbital motion of the water particle has a major impact on hydrodynamic forces (Teng, 1983). The method that represents waves using planar oscillatory flow neglects the free surface effects and vertical components of the water particle velocity. The drag and inertia coefficients are overpredicted when planar oscillatory flows are applied (Sarpkaya and Isaacson, 1981).

3.2.2. *Effects of roughness height and coverage ratio*

Fig. 9 shows the drag and inertia coefficients of the SFT configurations PR, PRS, and PS50 as a function of KC. It appears that both $C_{d,x}$ and $C_{d,z}$ increase exponentially with decreasing KC for the three configurations (Fig. 9(a∼b)). The largest $C_{d,x}$ and $C_{d,z}$ are found in the PR configuration compared to the PRS and PR50, demonstrating that $C_{d,x}$ and $C_{d,z}$ increase with increasing roughness height and coverage ratio. The disparities in $C_{d,x}$ and $C_{d,z}$ for all configurations, however, become smaller as KC increases. In the chosen wave conditions, the PRS configuration is more effective at reducing drag, compared to the PR50. Fig. 9(c) and (d) show that the $C_{m,x}$ and $C_{m,z}$ of the PR50 are the largest for wave-only conditions, and the difference in $C_{m,x}$ and $C_{m,z}$ between the PR and the PRS cases is small. As has been discussed in Section 4.2.1, surface roughness alleviates the inertia, and momentum is imparted as the flow interacts with roughness elements. As a result, with more roughness elements on the SFT surface, the PR and PRS cases have lower inertia coefficients than the PR50 configuration. Similarly, for all parametric shape configurations, $C_{m,x}$ and $C_{m,z}$ exhibit an increase,

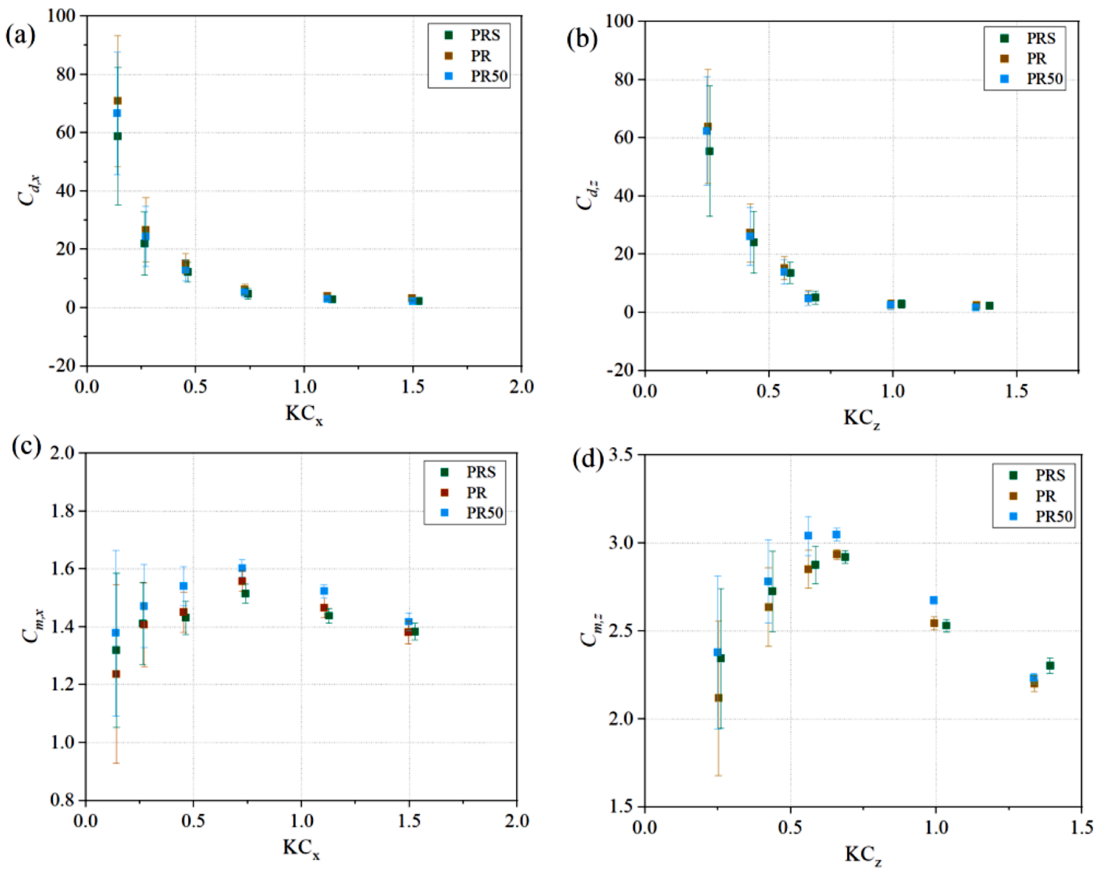

Fig. 9. Distribution of drag and inertia coefficients as a function of the Keulegan–Carpenter number KC (in the horizontal and vertical directions) for the SFT configuration PRS, PR, and PR50, under wave-only conditions.

followed by a decrease with maxima at KC = 0.7.

3.3. Combined current-wave conditions

Ocean waves typically exist together iwth currents. The kinematics and dynamics of the water particles are closely related to the hydrodynamic forces acting on the SFT, and the presence of currents has a substantial impact on these forces. This section presents results concerning combined current-wave conditions.

3.3.1. Effects of cross-section shape

The drag and inertia coefficients of the circular and parametric shapes (with the smooth and the rough SFT sets) are displayed in Fig. 10. The rough cases generally have a larger $C_{d,x}$ than the smooth cases. Contrary to the wave-only case, it is interesting to note that when KC$_x$ > 1.4, the circular shape (both rough and smooth configurations) has a larger $C_{d,x}$ than the parametric shape, and the difference of $C_{d,x}$ between the parametric shape and circular shape increases with increasing KC$_x$. This indicates that for KC$_x$ > 1.4, the cross-section shape (structural geometry) has a more significant impact on the drag under combined current-wave conditions than under the wave-only scenarios. The CR has the largest $C_{d,x}$ among the four SFT configurations. For the parametric shape (both smooth and rough cases), $C_{d,x}$ decreases with increasing KC$_x$, and the smooth case exhibits a larger negative slope than the rough one. However, for the circular shape (both smooth and rough cases), as KC$_x$ increases, $C_{d,x}$ undergoes a continuous drop followed by an increase, with a minimum at KC$_x$ = 4.8. This stems from the change in the current speed. The upstream current speed of the CW7 case (within the red block in Fig. 10(a)) is 0.3 m/s, whereas it is 0.2 m/s for the rest of the cases (CW1~CW6). It is interesting to note that, for the combined current-wave conditions, the increasing wave parameters (wave height and period) reduce $C_{d,x}$ (in cases CW1 ~ CW6), whereas the increasing current speed increases the horizontal drag (in cases CW6 ~ CW7). Similar to the wave-only cases, the parametric shape (in both rough and smooth sets) has a larger $C_{d,z}$ than the circular shape due to a longer horizontal dimension (Fig. 10(b)). For the same cross-section shape, the rough cases exhibit slightly larger $C_{d,z}$ than the smooth ones. However, the difference is minor. For all the SFT configurations, $C_{d,z}$ undergoes a sharp decrease with increasing KC$_z$ and when KC$_z$ reaches 0.6, $C_{d,z}$ begins to gradually stabilize at a value of about 1.0.

Regarding the inertia results, the parametric shape in Fig. 10(c) has a significantly lower $C_{m,x}$ than the circular shape, and the PR configuration has the lowest $C_{m,x}$. For the parametric shape, the difference in $C_{m,x}$ between the rough and the smooth cases is larger than for the circular shape. For all the SFT configurations, $C_{m,x}$ shows a declining trend as KC$_x$ increases., The parametric shape shows considerably larger $C_{m,z}$ than the circular shape (Fig. 10(d)). The difference in $C_{m,z}$ between the rough and the smooth cases for both cross-section shapes is not noticeable, indicating that the effect of roughness on the vertical inertia is negligible. Local maxima of $C_{m,z}$ for both shapes can be clearly seen at around KC$_z$ = 0.49. With increasing KC$_z$, $C_{m,z}$ gradually increases followed by a rapid decrease for the parametric shape, whereas it remains generally constant followed by a sharp decrease for the circular shape.

3.3.2. Effects of roughness height and coverage ratio

Fig. 11 shows the drag and inertia coefficients with the SFT configurations of the PR, PRS, and PS50 as a function of KC. Similar to the wave-only conditions, both $C_{d,x}$ and $C_{d,z}$ tend to increase with decreasing KC (Fig. 11(a) and (b)). The PR configuration has the largest $C_{d,x}$ and $C_{d,z}$, showing that under combined wave-current conditions, $C_{d,x}$ and $C_{d,z}$ increase with increasing roughness height and coverage ratio. However, the difference of $C_{d,x}$ and $C_{d,z}$ between the PRS and PR50 cases is not

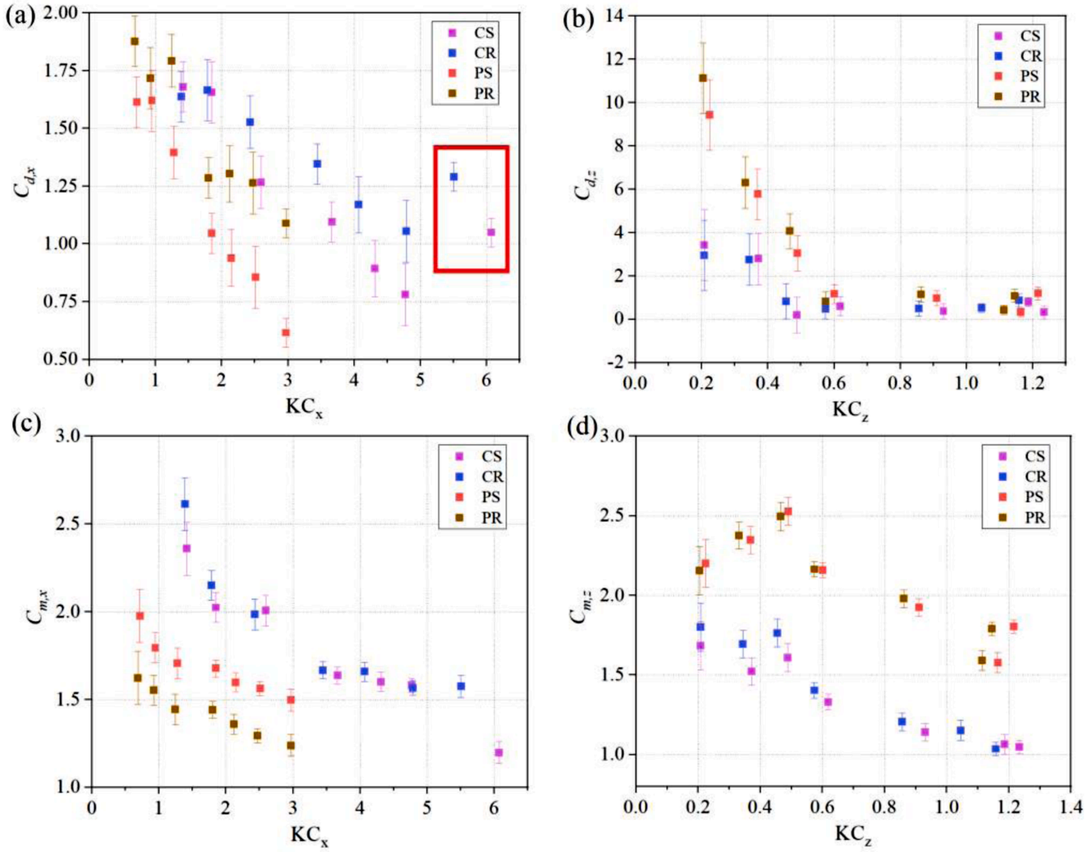

Fig. 10. Distribution of drag and inertia coefficients as a function of the Keulegan–Carpenter number KC (in the horizontal and vertical directions) for the SFT configuration CS, CR, PS, and PR, under combined current-wave conditions.

obvious, with the error bars overlapping.

As for the inertia coefficients (Fig. 11(c) and (d)), the differences in $C_{m,x}$ and $C_{m,z}$ among the three SFT configurations are minor, demonstrating that the roughness parameters are not key factors for the inertia coefficients under combined wave-current conditions. However, as KC increases, $C_{m,x}$ shows a continuously decreasing trend, but $C_{m,z}$ shows an increase and then a decrease with a maximum around $\mathrm{KC_z} = 0.49$ for all the SFT configurations.

4. Discussion

The hydrodynamic force coefficients of marine structures taking account of the marine growth effects are standardized in BS 6349-1-2 (2016), Veritas (2019), JTS-145-2-2013 (2013) and API (2014). However, the assessments of marine growth effects in such engineering standards are inconsistent and contentious. In order to provide recommendations for the SFT's engineering design with regard to the effects of marine fouling, the hydrodynamic force coefficients from this study and the existing standards are compared and evaluated.

The existing standards predict hydrodynamic forces mainly by applying the Morison equation with drag and inertia coefficients (C_d and C_m). The variation of the force coefficients can be accounted for by expressing C_d and C_m as a function of KC, Re, relative roughness ($\Delta = k/D$), etc. For the post-critical flow regime (high Re), the commonly applied approach of estimating C_d, shown in DNV-RP-C205 (Veritas, 2019), is given by

$$C_d = C_{DS}(\Delta)\cdot\psi(\mathrm{KC}) \tag{19}$$

where, $C_{DS}(\Delta)$is the roughness coefficient, for which the smooth and rough cylinder ($\Delta >$ 0.01) correspond to $C_{DS}(\Delta) =$ 0.65 and 1.05, respectively; $\psi(\mathrm{KC})$ is the wake amplification factor, given by

$$\psi(\mathrm{KC}) = \begin{cases} C_\pi + 0.10(\mathrm{KC} - 12), 2 \leq \mathrm{KC} < 12 \\ C_\pi - 1.00, 0.75 \leq \mathrm{KC} < 2 \\ C_\pi - 1.00 - 2.00(\mathrm{KC} - 0.75), \mathrm{KC} < 0.75 \end{cases} \tag{20}$$

where,

$$C_\pi = 1.50 - 0.024(12 / C_{DS} - 10) \tag{21}$$

The added mass coefficient C_A (= C_m - 1) is also associated with KC and $C_{DS}(\Delta)$, given by

$$C_A = \begin{cases} \max[1.0 - 0.44(\mathrm{KC} - 3), 0.6 - (C_{DS}(\Delta) - 0.65)], \text{for KC} > 3 \\ 1.0, \text{for KC} < 3 \end{cases} \tag{22}$$

For current-only scenarios, an infinite KC will cause C_d to asymptote to $C_{DS}(\Delta)$.

Similarly, in the API (API, 2014), C_d is regarded as a function of Re, KC, and Δ, and the plots of the dependence of steady flow$C_{DS}(\Delta)$ on KC and Δ in the post-critical regime are provided. In our case $k/D = 0.094$, and for the rough and smooth cylinders, $C_{DS}(\Delta)$ can be assumed as 1.1 and 0.6, respectively. For typical design situations, C_m approaches 2.0 for $\mathrm{K} \leq 3$ for both smooth and rough cylinders, while it decreases with increasing KC for $\mathrm{KC} > 3$.

However, in JTS-145-2-2013 (2013), for the smooth circular cylinder, C_d and C_m are assumed to be 1.2 and 2.0, respectively. The effect of KC is taken into account in the C_d and C_m computations for the combined current-wave scenarios, but only the data for $\mathrm{KC} \geq 5$ are accessible. For the marine fouling effect, the wave force is calculated by multiplying a scaling factor related to Δ. However, the marine fouling effects on C_d under current-only conditions are lacking.

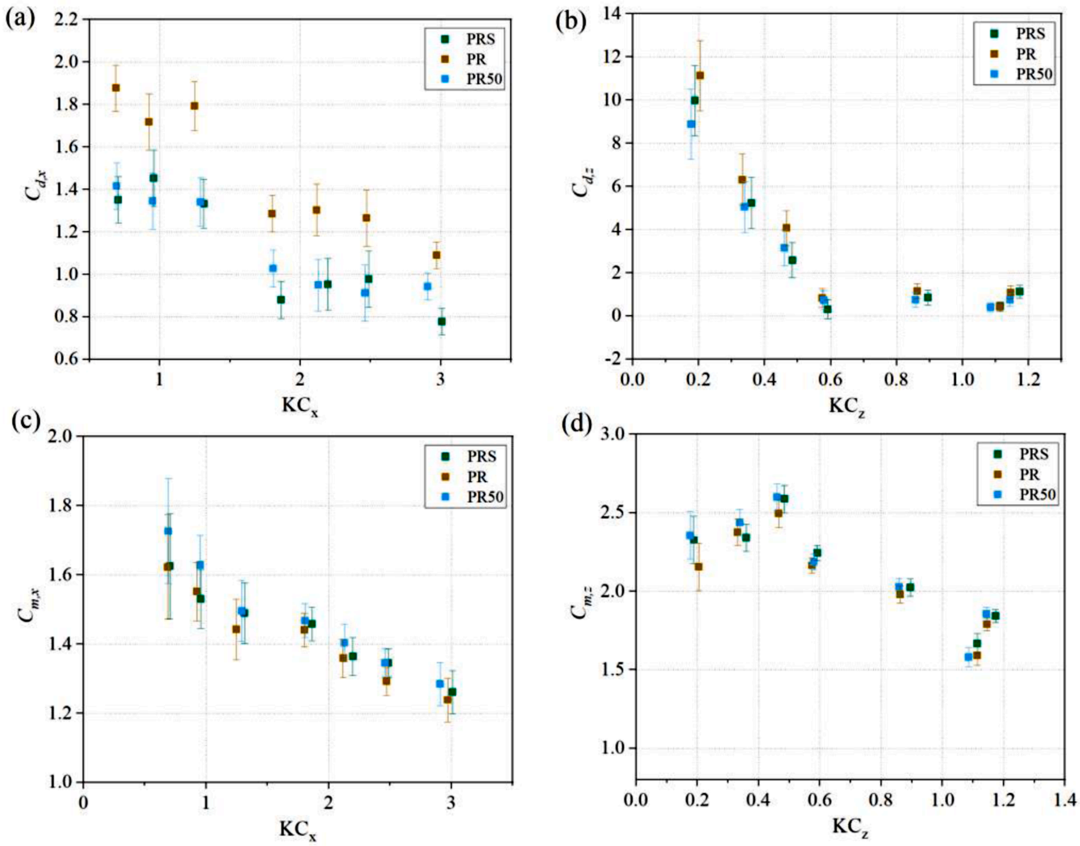

Fig. 11. Distribution of drag and inertia coefficients as a function of the Keulegan–Carpenter number KC (in the horizontal and vertical directions) for the SFT configuration PRS, PR, and PR50, under combined current-wave conditions.

Since no suitable value can be provided from the standards for the parametric shape, the comparison between the calculated C_d and C_m from the experiments and the predictions from the engineering standards for the CS and CR configurations under current-only and combined current-wave conditions is presented in Fig. 12(a). It shows that for both the smooth and rough cases under current-only conditions, all the selected engineering standards underestimate C_d. The DNV and API (Veritas, 2019; API, 2014) predictions for the smooth cylinder are lower than the JTS's results.

For the combined current-wave conditions, C_d is considerably underpredicted by all the standards, and an inverse relationship between C_d and KC is shown in the API and DNV[53], (Veritas, 2019) predictions compared to the measured results (Fig. 12(b)). However, despite only the result at KC $\geq$ 5 being available in JTS, the predictions of C_d for both the smooth and rough cylinders show good agreements with the measured data. Regarding the C_m (Fig. 12(c)), in the selected range of KC, there is no dependence of C_m on the surface roughness in the standards' results, and a generally constant value of C_m around 2 is provided in API and DNV. However, as KC increases, C_m shows a decreasing trend in the measured data. Since JTS multiplies wave force by a large factor when it accounts for marine growth, C_m is significantly overestimated for the rough case. For all the scenarios, the predictions from DNV and API (Veritas, 2019; API, 2014) are comparable for both the smooth and rough cases because an identical approach is adopted for determination of the force coefficients.

The differences highlighted in the comparison stem from various reasons. For a horizontal cylinder in waves, the vertical component of the water particle velocity is crucial, and the Morison equation should be

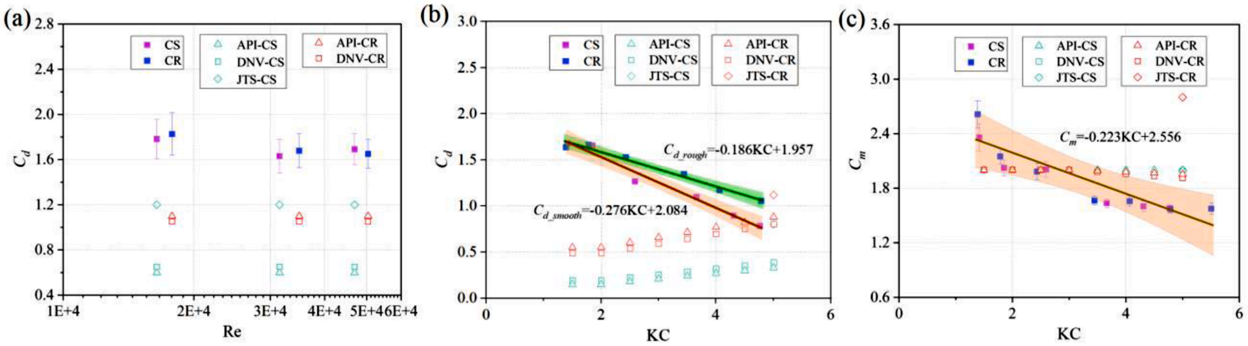

Fig. 12. Comparison between the predictions of the drag and the inertia coefficients between the engineering standards and the experimental data. (a) C_d under current-only conditions; (b) C_d under combined curren-wave conditions; (c) C_m under combined current-wave conditions.

modified into a vector form. However, most of the standards are based on vertical cylinders such as riser segments in Veritas (2019), platforms in API (2014), and vertical piles in JTS-145-2-2013 (2013).

Furthermore, the hydrodynamic force coefficients are mostly provided for the post-critical regime by the current standards. However, in this study, the smooth cylinder is in the subcritical regime. The variation of hydrodynamic force coefficients on a cylinder is very pronounced for different flow regimes.

In addition, to account for the marine growth effects, the equivalent diameter of the structural elements applied in BS 6349-1-2 (2016), Veritas (2019), API (2014) adopts a “clean” outer cylinder diameter plus twice the thickness of marine growth, while in JTS-145-2-2013 (2013), the wave force computation takes into account the bare cylinder diameter and a scaling factor. However, in this study, an equivalent diameter with an equal blockage area is adopted for the rough cases. This definition manifests in the normalized parameters such as Reynolds number, drag and lift coefficients, and Strouhal number, and it, therefore, affects the hydrodynamic force coefficient predictions. It is also noteworthy that the current engineering standards for maritime structures that account for the effects of marine biofouling are typically based on empirical formulas or defined values (BS 6349-1-2, 2016; Veritas, 2019; JTS-145-2-2013, 2013; API, 2014), with a limited number of roughness characteristics considered (e.g., roughness thickness).

Finally, blockage effects have a significant influence on the hydrodynamic forces, which are not adequately taken into account in those engineering standards. The blockage ratio affects the pressure distribution and flow separation by restricting the wake flow. As the blockage ratio increases, the local flow velocity is enhanced and thus, increases the local Reynolds number. The higher blockage acts to decrease the inertia coefficient of the in-line force exerted on the cylinder and to increase the drag coefficient (Anagnostopoulos and Minear, 2004). The blockage effects need to be carefully considered if the blockage is over 6% (West and Apelt, 1982).

In order to provide a reference for the SFT’s hydrodynamic force coefficients with consideration for marine growth effects, regression analysis is performed for the smooth and rough cases based on the measured data, shown in Fig. 12. Each fitting has a designated confidence band. For the current-only condition, the difference between the rough and the smooth case is minor, and thus, $C_d = 1.75 \pm 0.15$ is recommended. Regarding the combined current-wave conditions for $1 < \mathrm{KC} < 5$, the hydrodynamic force coefficients are given by Eqs. (23)~(24)

$$\begin{cases} C_d = -0.276\mathrm{KC} + 2.084, \text{for smooth cylinders} \\ C_d = -0.186\mathrm{KC} + 1.957, \text{for rough cylinders} \end{cases} \tag{23}$$

$$C_m = -0.223\mathrm{KC} + 2.556 \tag{24}$$

5. Conclusions

This paper presents an experimental study of marine fouling (represented by surface roughness) effects on the hydrodynamic forces and flow characteristics of the SFT under various types of environmental conditions (i.e., current-only, wave-only, and combined current-wave conditions). The influence of cross-section shape and roughness parameters including roughness height and roughness coverage ratio on the hydrodynamic force coefficients of the SFT is assessed. The measured hydrodynamic force coefficients based on the Morison equation for the smooth and rough SFTs are compared against predictions from existing engineering standards for other marine structures, and recommendations for the hydrodynamic force coefficients for the SFT are provided with consideration of blockage effects and the definition of the equivalent diameter of the structure. The main findings are summarized as follows:

(1) For current-only conditions, compared to the circular shape, the parametric shape can effectively lower C_d due to the streamlined shape; however, the drag reduction caused by shape optimization is less prominent in the presence of surface roughness. The C_d of the SFT increases with increasing roughness height and coverage ratio. Large roughness elements can result in incoherence of the vortices, homogenization of the turbulent flow, and reduction of the peak force amplitude of the frequency spectrum.

(2) For wave-only conditions, the parametric shape for both smooth and rough cases has a much lower $C_{m,x}$ than the circular shape, and the parametric shape is particularly susceptible to the effects of exaggerated surface roughness. The friction drag can be increased by the parametric shape due to its longer perimeter. Due to the longer horizontal dimension and larger cross-sectional area of the parametric shape, the vertical hydrodynamic force coefficients are generally larger than the circular shape. Roughness parameters do not have a strong effect on C_d and C_m for wave-only conditions.

(3) For combined current-wave conditions, similar to the wave-only conditions, the parametric shape has a much smaller $C_{m,x}$ than the circular shape, while the vertical force coefficients are larger. Contrary to the wave-only cases, it is more evident under wave-current combined conditions that C_d increases with increasing roughness height and coverage ratio, indicating the steady current component has a substantial influence.

(4) Based on the Morison equation, the current engineering standards used for marine structures such as risers and pipelines are unable to provide plausible prediction of hydrodynamic force coefficients for an SFT. For an SFT with a blockage ratio of 23%, the measured drag coefficient can increase substantially (up to 50%). The SFT, with its unique characteristics such as large blockage and low KC, should be carefully reevaluated in light of marine fouling effects.

The findings of this study aid in a better understanding of marine fouling effects on the hydrodynamic behavior of the SFT in the presence of waves and currents. The evolution of hydrodynamic coefficients as a function of the various environmental conditions reveals a close correlation between hydrodynamic loads, structural geometry, and roughness parameters. The evaluated findings of hydrodynamic force in relation to structural geometry and roughness parameters can provide references for the engineering design of SFTs. However, the applied regular pyramidal roughness only very roughly represents actual marine fouling organisms. Further research is required to determine the impacts of a roughness that is more realistically shaped and proportioned, as well as the distribution and colonization patterns of marine fouling.

CRediT authorship contribution statement

P.X. Zou: Conceptualization, Methodology, Formal analysis, Validation, Visualization, Writing – original draft. **N. Ruiter:** Methodology, Investigation, Formal analysis, Validation, Data curation, Writing – review & editing. **W.S.J. Uijttewaal:** Conceptualization, Methodology, Formal analysis, Supervision. **X.X. Chen:** Conceptualization, Methodology. **D.J. Peters:** Project administration. **J.D. Bricker:** Methodology, Formal analysis, Supervision, Writing – review & editing.

Declaration of Competing Interest

The authors declare that they have no known competing financial interests or personal relationships that could have appeared to influence the work reported in this paper.

Data availability

Data will be made available on request.

Acknowledgment

The study presented in this paper was conducted in the submerged floating tunnel research project funded by China Communications Construction Company Ltd. (CCCC). Funding for reporting was partially obtained from the Cooperative Institute for Great Lakes Research (CIGLR) postdoctoral fellowship.

References

Achenbach, E., Heinecke, E., 1981. On vortex shedding from smooth and rough cylinders in the range of Reynolds numbers 6×103 to 5×106. J. Fluid Mech. 109 (12) https://doi.org/10.1017/S002211208100102X.

Allen, H.J., Vincenti, W.G., 1944. Wall interference in a two-dimensional-flow wind tunnel, with consideration of the effect of compressibility. NACA Rep. 30 (782).

Ameryoun, H., Schoefs, F., Barillé, L., Thomas, Y., 2019. Stochastic modeling of forces on jacket-type offshore structures colonized by marine growth. J. Mar. Sci. Eng. 7 (5) https://doi.org/10.3390/jmse7050158.

Anagnostopoulos, P., Minear, R., 2004. Blockage effect of oscillatory flow past a fixed cylinder. Appl. Ocean Res. 26 (3–4) https://doi.org/10.1016/j.apor.2004.11.001.

API, 2014. API 2A-WSD: Recommended practice for planning, designing and constructing fixed offshore platforms-working stress design. American Petroleum Institute.

Bai, J., Ma, N., Gu, X., 2017. Study of interaction between wave-current and the horizontal cylinder located near the free surface. Appl. Ocean Res. 67 https://doi.org/10.1016/j.apor.2017.06.004.

Blackburn, H.M., Melbourne, W.H., 1996. The effect of free-stream turbulence on sectional lift forces on a circular cylinder. J. Fluid Mech. 306 https://doi.org/10.1017/S0022112096001309.

Chandler, B.D., Hinwood, J.B., 1982. Combined wave-current forces on horizontal cylinders. Coast. Eng. Proc. (18), 130.

Chaplin, J.R., 1988. Loading on a cylinder in uniform oscillatory flow: part I- Planar oscillatory flow. Appl. Ocean Res. 10 (4).

Demirel, Y.K., Uzun, D., Zhang, Y., Fang, H.C., Day, A.H., Turan, O., 2017. Effect of barnacle fouling on ship resistance and powering. Biofouling 33 (10). https://doi.org/10.1080/08927014.2017.1373279.

BS 6349-1-2, 2016. Maritime works: General...Code of Practice for Assessment of Actions. British Standards Institute. London, UK.

Drost, L., 2019. The submerged floating tunnel: an experimental study on the hydrodynamics and kinematics of a submerged rectangular cylinder in a wave-current environment. Delft University of technology.

Fredsoe, J., Sumer, B.M., 2006. Hydrodynamics around cylindrical structures (revised edition), 26. World Scientific.

Fuss, F.K., 2011. The effect of surface skewness on the super/postcritical coefficient of drag of roughened cylinders. Proc. Eng. 13 https://doi.org/10.1016/j.proeng.2011.05.086.

Henry, P.Y., Nedrebø, E.L., Myrhaug, D., 2016. Visualisation of the effect of different types of marine growth on cylinders' wake structure in low Re steady flows. Ocean Eng. 115 https://doi.org/10.1016/j.oceaneng.2016.02.023.

il Seo, S., suk Mun, H., ho Lee, J., ha Kim, J., 2015. Simplified analysis for estimation of the behavior of a submerged floating tunnel in waves and experimental verification. Mar. Struct. https://doi.org/10.1016/j.marstruc.2015.09.002.

Iwagaki, Y., Asano, T., 1985. Hydrodynamic forces on a circular cylinder due to combined wave and current loading. In: Proceedings of the Coastal Engineering Conference, 3. https://doi.org/10.1061/9780872624382.192.

Jusoh, I., Wolfram, J., 1996. Effects of marine growth and hydrodynamic loading on offshore structures. Jurnal Mekanikal 1 (1), 77–96.

JTS-145-2-2013, 2013. Code of hydrology for sea harbour. Ministry of Transport of the People's Republic of China.

Justesen, P., 1989. Hydrodynamic forces on large cylinders in oscillatory flow. J. Waterw. Port Coastal Ocean Eng. 115 (4) https://doi.org/10.1061/(asce)0733-950x(1989)115:4(497).

Konstantinidis, E., Bouris, D., 2017. Drag and inertia coefficients for a circular cylinder in steady plus low-amplitude oscillatory flows. Appl. Ocean Res. 65 https://doi.org/10.1016/j.apor.2017.04.010.

Mansard, E.P.D., Funke, E.R., 1980. The measurement of incident and reflected spectra using a least squares method. Coast. Eng. Proc. 1 (17) https://doi.org/10.9753/icce.v17.8.

Marty, A., et al., 2021a. Effect of roughness of mussels on cylinder forces from a realistic shape modelling. J. Mar. Sci. Eng. 9 (6), 598.

Marty, A., et al., 2021b. Experimental study of hard marine growth effect on the hydrodynamical behaviour of a submarine cable. Appl. Ocean Res. 114 https://doi.org/10.1016/j.apor.2021.102810.

Marty, A., Schoefs, F., Damblans, G., Facq, J.V., Gaurier, B., Germain, G., 2022. Experimental study of two kinds of hard marine growth effects on the hydrodynamic behavior of a cylinder submitted to wave and current loading. Ocean Eng. 263, 112194.

Morison, J.R., Johnson, J.W., Schaaf, S.A., 1950. The force exerted by surface waves on piles. J. Pet. Technol. 2 (05) https://doi.org/10.2118/950149-g.

Pearcey, T., Zhao, M., Xiang, Y., Liu, M., 2017. Vibration of two elastically mounted cylinders of different diameters in oscillatory flow. Appl. Ocean Res. 69 https://doi.org/10.1016/j.apor.2017.11.003.

Ribeiro, J.D., 1991. Effects of surface roughness on the two-dimensional flow past circular cylinders I: mean forces and pressures. J. Wind Eng. Ind. Aerodyn. 37 (3) https://doi.org/10.1016/0167-6105(91)90014-N.

Richter, A., Naudascher, E., 1976. Fluctuating forces on a rigid circular cylinder in confined flow. J. Fluid Mech. 78 (3) https://doi.org/10.1017/S0022112076002607.

Roshko, A., 1961. Experiments on the flow past a circular cylinder at very high Reynolds number. J. Fluid Mech. 10 (3) https://doi.org/10.1017/S0022112061000950.

Rusch, C.J., Mundon, T.R., Maurer, B.D., Polagye, B.L., 2020. Hydrodynamics of an asymmetric heave plate for a point absorber wave energy converter. Ocean Eng. 215 https://doi.org/10.1016/j.oceaneng.2020.107915.

Sarpkaya, T., Isaacson, M., 1981. Mechanics of wave forces on offshore structures.van. Nostrand Reinhold, NewYork.

Schewe, G., 1983. On the force fluctuations acting on a circular cylinder in crossflow from subcritical up to transcritical Reynolds numbers. J. Fluid Mech. 133 https://doi.org/10.1017/S0022112083001913.

Schoefs, F., Ameryoun, H., 2013. Probabilistic modeling of the bio-colonization effects on hydrodynamic forces with several combinations of sea-state condition: a study on jacket-platforms in the gulf of Guinea. In: Proceedings of the International Conference on Offshore Mechanics and Arctic Engineering - OMAE, 1. https://doi.org/10.1115/OMAE2013-11100.

Schoefs, F., Bakhtiari, A., Ameryoun, H., 2022. Evaluation of hydrodynamic force coefficients in presence of biofouling on marine/offshore structures, a review and new approach. J. Mar. Sci. Eng. 10 (5), 558.

Schultz, M.P., 2007. Effects of coating roughness and biofouling on ship resistance and powering. Biofouling 23 (5). https://doi.org/10.1080/08927010701461974.

Skomedal, N.G., Vada, T., Sortland, B., 1989. Viscous forces on one and two circular cylinders in planar oscillatory flow. Appl. Ocean Res. 11 (3) https://doi.org/10.1016/0141-1187(89)90022-9.

Sun, C., Zhou, T., An, H., Zhu, H., Cheng, L., 2020. Effect of surface roughness heights on circular cylinder wakes. In: Proceedings of the 22nd Australasian Fluid Mechanics Conference, AFMC2020. https://doi.org/10.14264/3eb5472.

Teng, C.C., 1983. Hydrodynamic forces on a horizontal cylinder under waves and current. MSc. Oregon State University.

Theophanatos, A., Wolfram, J., 1989. Hydradynamic loading on macro-roughened cylinders of warious aspect ratios. J. Offshore Mech. Arct. Eng. 111 (3) https://doi.org/10.1115/1.3257150.

Veritas, N., 2019. *Environmental conditions and environmental loads*. Det Norske Veritas, Oslo, Norway.

Walker, J.S., Green, R.B., Gillies, E.A., Phillips, C., 2020. The effect of a barnacle-shaped excrescence on the hydrodynamic performance of a tidal turbine blade section. Ocean Eng. 217 https://doi.org/10.1016/j.oceaneng.2020.107849.

West, G.S., Apelt, C.J., 1982. The effects of tunnel blockage and aspect ratio on the mean flow past a circular cylinder with Reynolds numbers between 104 and 105. J. Fluid Mech. 114 https://doi.org/10.1017/S0022112082000202.

Wikipedia, 2023. Submerged floating tunnel. https://en.wikipedia.org/wiki/Submerged_floating_tunnel.

Wu, Z., Wang, D., Ke, W., Qin, Y., Lu, F., Jiang, M., 2021. Experimental investigation for the dynamic behavior of submerged floating tunnel subjected to the combined action of earthquake, wave and current. Ocean Eng. 239 https://doi.org/10.1016/j.oceaneng.2021.109911.

Yang, Z., et al., 2023. Experimental study on the wave-induced dynamic response and hydrodynamic characteristics of a submerged floating tunnel with elastically truncated boundary condition. Mar. Struct. 88, 103339.

Zdravkovich, M.M., 1996. Inadequacy of a conventional Keulegan–Carpenter number for wave and current combination. J. Offshore Mech. Arct. Eng. 118 (4) https://doi.org/10.1115/1.2833922.

Zeinoddini, M., Bakhtiari, A., Ehteshami, M., Seif, M.S., 2016. Towards an understanding of the marine fouling effects on VIV of circular cylinders: response of cylinders with regular pyramidal roughness. Appl. Ocean Res. 59 https://doi.org/10.1016/j.apor.2016.05.013.

Zhou, B., Wang, X., Gho, W.M., Tan, S.K., 2015. Force and flow characteristics of a circular cylinder with uniform surface roughness at subcritical Reynolds numbers. Appl. Ocean Res. 49 https://doi.org/10.1016/j.apor.2014.06.002.

Zou, P., Bricker, J., Uijttewaal, W., 2020a. Optimization of submerged floating tunnel cross section based on parametric Bézier curves and hybrid backpropagation - genetic algorithm. Mar. Struct. https://doi.org/10.1016/j.marstruc.2020.102807.

Zou, P., Bricker, J.D., Uijttewaal, W., 2021a. Submerged floating tunnel cross-section analysis using a transition turbulence model. J. Hydraul. Res. https://doi.org/10.1080/00221686.2021.1944921.

Zou, P.X., Bricker, J.D., Chen, L.Z., Uijttewaal, W.S.J., Ferreira, C.S., 2022. Response of a submerged floating tunnel subject to flow-induced vibration. Eng. Struct. 253 https://doi.org/10.1016/j.engstruct.2021.113809.

Zou, P.X., Bricker, J.D., Uijttewaal, W., 2020b. A parametric method for submerged floating tunnel cross-section design. In: Proceedings of the International Offshore and Polar Engineering Conference.

Zou, P.X., Bricker, J.D., Uijttewaal, W.S.J., 2020c. Impacts of extreme events on hydrodynamic characteristics of a submerged floating tunnel. Ocean Eng. 218 https://doi.org/10.1016/j.oceaneng.2020.108221.

Zou, P.X., Bricker, J.D., Uijttewaal, W.S.J., 2021b. The impacts of internal solitary waves on a submerged floating tunnel. Ocean Eng. 238, 109762.

Zou, P.X., Chen, L.Z., 2021. The Coupled Tube-Mooring System SFT Hydrodynamic Characteristics Under Wave Excitations. In: Proceedings of the 14th International Conference on Vibration Problems: ICOVP 2019, pp. 907–923.

Zou, P.X., Ruiter, N., Bricker, J.D., Uijttewaal, W.S.J., 2023. Effects of roughness on hydrodynamic characteristics of a submerged floating tunnel subject to steady currents. Mar. Struct. 89, 103405 https://doi.org/10.1016/j.marstruc.2023.103405. May.